ARTICLE

Received 00th January 20xx,

Accepted 00th January 20xx

DOI: 10.1039/x0xx00000x

High strength hydrogels enable dendrite-free Zn metal anodes and high-capacity Zn-MnO_2 batteries via a modified mechanical suppression effect

Ruijie Zhu, [a] *Huijun Yang,* [b] *Wei Cui,* [c] *Laras Fadillah,* [a] *Tianhong Huang,* [d] *Zetao Xiong,* [a] *Chunmei Tang ,* [a] *Damian Kowalski,* [e] *Sho Kitano,* [a,f] *Chunyu Zhu*,* [g] *Daniel R. King*,* [c] *Takayuki Kurokawa,* [c] *Yoshitaka Aoki,* [a,f] *and Hiroki Habazaki.* [a,f]

ABSTRACT Rechargeable aqueous zinc-ion batteries (RAZIBs) have some inherent advantages such as intrinsic safety, low-cost and theoretically high energy density, making them a current topic of interest. However, the phenomenon of zinc (Zn) dendrite growth at the anode results in the instability of RAZIBs and limits their real-world application. Herein, by employing a high strength hydrogel polymer electrolyte, the growth of dendritic Zn crystals is effectively eliminated through the mechanical suppression effect, resulting in a stable Zn anode that demonstrates dendrite-free plating/stripping with a long lifespan. Even under a high current density of 5 mA cm^{-2}, the Zn || Zn symmetric cell is shown to have a cyclic lifetime of longer than 1000 hours. Moreover, the stable cyclic performance of the Zn anode spawns a Zn || MnO_2 battery with high capacity (4.8 mAh cm^{-2} – 1.9 mAh cm^{-2}) and long lifetime (500 cycles at 9.2 mA cm^{-2}, 1 C), which can meet the practical demands for portable devices. This work introduces that high strength polymer gel electrolytes with internal energy dissipation mechanisms can overcome previous challenges that prevented practical utilization of RAZIBs. Together with the outstanding cyclic properties of the high capacity Zn || MnO_2 batteries, this work provides a new pathway toward designing high energy density RAZIBs.

1. Introduction

Rechargeable aqueous zinc-ion batteries (RAZIBs) are attractive portable power sources for achieving both safe energy storage devices and building clean and sustainable energy systems.[1, 2] Current high-energy-density lithium-ion batteries (LIBs) have high energy storage costs due to the limited availability of lithium (Li) and the requirement of expensive organic electrolytes, and are known to have significant safety problems. [3-5] In contrast, zinc (Zn) metal is inexpensive and RAZIBs do not rely on organic electrolytes. At the same time, Zn metal has a very high capacity and a low negative potential (820 mAh g^{-1} or 5855 mAh cm^{-3}, −0.76 V vs. Standard Hydrogen Electrode),[6, 7] and is also stable in air, which makes rechargeable batteries based on Zn metal anodes an appealing alternative to conventional energy storage devices.[8]

A problem that limits the lifespan of RAZIBs and prevents their usage is that dendritic growth of Zn during electrodeposition will

[a] *Graduate School of Chemical Sciences and Engineering, Hokkaido University, Sapporo, Hokkaido 060-8628, Japan*
[b] *National Institute of Advanced Industrial Science and Technology (AIST), 1-1-1, Umezono, Tsukuba 305-8568 Japan.*
[c] *Faculty of Advanced Life Science, Hokkaido University, Sapporo 001-0021, Japan. E-mail: dking@sci.hokudai.ac.jp*
[d] *Department of Mathematics, University of Wisconsin Madison, Madison, WI, 53705, USA*
[e] *Faculty of Chemistry and Biological and Chemical Research Centre, University of Warsaw, Zwirki i Wigury 101, 02-089 Warsaw, Poland.*
[f] *Division of Applied Chemistry, Faculty of Engineering, Hokkaido University, Sapporo, Hokkaido 060-8628, Japan*
[g] *School of Electrical and Power Engineering, China University of Mining and Technology, Xuzhou 221116, China*
E-mail: zcyls@cumt.edu.cn

Correspondence to zcyls@cumt.edu.cn (C. Zhu)
dking@sci.hokudai.ac.jp (D. R. King)
† Footnotes relating to the title and/or authors should appear here. Electronic Supplementary Information (ESI) available: [details of any supplementary information available should be included here]. See DOI: 10.1039/x0xx00000x

occur in neutral or alkaline aqueous solutions.[9, 10] Different from alkali metals (i.e. lithium, sodium, potassium), where dendritic growth is mainly attributed to the uneven distribution of the ion-flux, the growth of Zn dendrites generally starts from the deposition of Zn with preferred crystal orientation. The subsequent deposition of Zn crystals occurs along the identical crystal lattice as the pre-deposited Zn nucleus, magnifying the uneven distribution of the ion-flux and resulting in the formation of large dendrites. Even worse, the dendritic growth during Zn plating can be extremely aggressive when the electrode is working at a high current density with a high areal capacity. Because of these problems it is difficult to achieve rechargeable Zn metal batteries that are safe and reliable energy storage devices with high energy density. [11-13] Therefore, current RAZIB technologies are still immature and requires significant advances to enable their use in fields where they could excel, such as in flexible electronics. [14-18]

Current efforts that have been attempted to limit the growth of Zn dendrites have mainly focused on two aspects: 1) considering that the dendritic growth of metals in an electrodeposition process can be depicted by the Sand's time model, [19, 20] some researchers believed that by regulating the Zn-ion flux and reducing the local current density, the growth of Zn dendrites could be delayed, resulting in a relatively uniform distribution of Zn deposition; [6, 21-25] 2) others have pointed out that by optimizing the orientation of Zn metal during electrodeposition, the shape of the deposited Zn crystals can be nonaggressive, because a substrate with specific crystal symmetry and lattice parameters would facilitate heterogeneous nucleation.[26-29] The heterogeneous nucleation of Zn may lead to "homoepitaxial deposition" in the subsequent electrodeposition process, and thus a uniform metal plating layer could be achieved.

Solid-state electrolytes (SSEs) with high modulus show excellent dendrite suppression capability in alkali metal batteries.[30-32] Recently, Hong et. al. pointed out that mechanically strong gel polymer electrolytes (GPEs) have the potential to limit the growth of Zn dendrites.[33] In Hong's model, the volume change induced by the electrodeposited Zn atoms causes the Zn to interact with the GPE at the interface. The combination of the volume strain of the GPE and their bulk modulus is considered an additional stress to inhibit Zn crystal growth. Additional stress on the Zn crystals causes a reduction in the exchange current density, and thereby forced uniform Zn metal deposition could be achieved.[34] It is commonly accepted that dendritic growth can be suppressed when a separator has a shear modulus 1.8 times higher than the anode metal. [35] The shear modulus of Li is 4.9 GPa, while Zn has a higher value of 38.8 GPa. Different from alkali metals, the modulus of Zn metal is very high, and conventional soft materials are not expected to possess Zn dendrite growth restricting properties. Therefore, investigating whether novel, stiff GPEs are capable of limiting Zn dendrite growth is necessary. Furthermore, understanding why these materials can overcome previous theoretical limitations is a requirement in order to enable next-generation RAZIBs.

Here, we report the utilization of high strength hydrogels as GPEs for efficiently suppressing Zn dendrite growth, with the ultimate goal of achieving high efficiency energy storage based on RAZIBs. By a two-step polymerization method, a double network (DN) hydrogel consisting of poly(2-acrylamido-2-methylpropanesulfonicacid)/polyacrylamide (PAMPS/PAM), which is embedded with a glass fiber (GF) skeleton, was prepared. The glass fiber-supported double network hydrogel (DNGF) shows high Young's modulus in both compression and tension, which is several times higher than the best previously reported GPEs (Table S1, Table S2 and Table S5). The DNGF was used as a GPE for suppressing Zn dendrite formation. The superior mechanical strength of DNGF can eliminate the growth of Zn dendrites, forcing Zn to grow along the electrode surface, resulting in a flat Zn plating layer. At the same time, the high ionic conductivity of the DNGF-based GPE can also reduce the concentration polarization on the electrode surface, enabling the Zn anode to achieve cycle stability over thousands of hours with a low overpotential. Based on these results, a high-capacity Zn || MnO_2 battery that can effectively avoid short circuits has been developed. The successful use of the high strength GPE provides a new route to design a separator that can prevent dendrite growth and shows excellent potential for achieving high energy density RAZIBs.

2. Results and Discussion

2.1 Preparation of the high strength hydrogel polymer electrolyte.

Figure 1a and **Figure S1** shows the schematic diagram of the DNGF preparation. 2-acrylamido-2-methylpropanesulfonic acid (AMPS) and the cross-linker N,N'-Methylenebisacrylamide (MBAA) were firstly dissolved in water, and a piece of glass fiber separator was immersed in this solution. The glass fiber has a non-woven structure with a fiber diameter range of 0.5 - 2 μm (**Figure S2**). Then, the glass fiber with AMPS was placed under ultraviolet (UV) light to achieve the gelation of AMPS. Here, the glass fiber sheet was used as a skeleton to support the fragile PAMPS, which plays an important role in subsequent experiments. The obtained composite that consists of PAMPS and glass fiber was coded as PAMPS-GF. After that polyacrylamide (PAM) solution swelled the structure of PAMPS-GF, and a second UV polymerization resulted in a PAMPS-PAM double network hydrogel containing glass fiber, which was coded as DNGF. During deformation of the DNGF, sacrificial rupture of the first network (PAMPS-GF) dissipates energy prior to global gel fracture.[36, 37] The occurrence of sacrificial fracture can be observed during tensile testing by the presence of a yield stress, denoted by the blue arrow in **Figure 1b**. The entanglement between polymer strands from of the first network and the second network provides stress transfer between the two networks, enabling high strength of the DNGF. Thus, the DNGF could be stretched to a length that was 10 times longer than its original size, while a high stress was maintained. As a comparison, the single network (SN) PAM hydrogel and the PAM-GF composite hydrogel (see preparation details in the supporting information) are also capable of achieving high strain but only show very low stress during tensile testing. PAMPS, as a polyelectrolyte, swells to many times its initial volume in water and is extremely brittle. Similarly the PAMPS-GF can only sustain up to 5.5% strain prior to failure. [38] The stress-strain curves of the gels under compression are compared in **Figure 1c and Figure S3**. The DNGF can sustain a stress of 6.9 MPa at a strain of 80%, which is 10 times higher than the PAM SN gels. **Figure 1d,e** illustrate the straightforward tests of how the DNGF sustains a high compression or a high stretch, while **Figure 1f** shows the optical morphology of the translucent DNGF sample. In order to further understand the superiority in mechanical properties of DNGF, we

summarized the shear modulus of the GPEs in Table S1. We clearly see that the DNGF has a shear modulus significantly higher than most conventional hydrogels and is more than an order of magnitude stiffer than either of its neat components (Table S2). These results indicate that the mechanical properties of the newly developed DNGF is sufficient to be termed as high-strength GPE for ZIBs.

2.2 Verification of the modified mechanical suppression effect of DNGF on Zn dendrite growth.

In order to verify the effect of high strength GPE on the electrodeposition of Zn metal, the dried DNGF was firstly swollen by a $ZnSO_4$ aqueous solution (2 mol L^{-1}) to prepare the semi-solid hydrogel electrolyte.[39, 40] The obtained GPE showed a high ionic conductivity of 26.8 mS cm^{-1} (**Figure S4** in supporting information). The DNGF GPE was then placed in a two-electrode Zn || Zn cell with the configuration shown in **Figure 2a**. We first examined the deposition behavior of Zn metal at a constant current density. As shown in **Figure 2b**, when Zn metal was galvanostatically deposited on a planar Zn foil without a separator, Zn dendrites would grow at the very initial plating stage and rapidly expanded without any limitation. This observation shows that even in an aqueous electrolyte with extremely high Zn^{2+} diffusion coefficient, $D_{(Zn^{2+})}$, and excellent ionic conductivity, the growth of zinc dendrites can still be very aggressive, which is very different from the cases observed in Li metal anodes[41-47]. The dendrite growth of Li could be efficiently alleviated by optimizing the mobility of Li^+. When DNGF was used as the GPE, as shown in **Figure 2c**, no formation of Zn dendrites could be observed. In this case, the pictures obtained from the small optical observation window indicate that the Zn coating layer gradually thickened. The electroplated Zn electrode was then taken out after the test, and it was found that the plating-layer was very uniform, as shown in **Figure S5**. High capacity galvanostatic plating tests were also conducted. Zn || Zn symmetric cells were assembled with a GF separator or DNGF, respectively. Zn was plated at a current density of 1 mA cm^{-2} for 16 h. For the Zn || Zn cell that used a GF separator, a short-circuit was observed after Zn deposition to a capacity of ~10.5 mA h cm^{-2} (**Figure 2d**). A large Zn dendrite with a length of about ~0.29 mm was observed by scanning electron microscopy (SEM, **Figure 2e**). It is conceived that the large Zn dendrite caused the internal short-circuit of the cell. The root reason of this dendrite formation can be traced back to the extremely uneven deposition of Zn. As shown in **Figure 2f**, the top view of the Zn plated electrode exhibits a disorganized morphology that consists of bare Zn plates and spherical Zn crystals. The top of the spherical Zn crystals was extensively covered with large and sharp Zn flakes (**Figure 2g**), which is representative of Zn metal that is preferentially deposited along the [100], and [101] crystal planes in the aqueous electrolyte.[48, 49] When the Zn || Zn cell was separated by the DNGF GPE, a stable plating process was achieved during Zn deposition (**Figure 2h**). The recorded overpotential of the cell was from ~160 mV at the initial stage and gradually reduced to a stable value of ~ 65 mV. Because of the sluggish transfer of Zn^{2+} in the hydrogel electrolyte, both the initial overpotential and the overpotential platform in the DNGF separated cell were slightly higher than the values of the GF separated Zn || Zn cell. The top view of the Zn plated electrode, which is shown in **Figure 2i**, shows that the surface was covered by even and dense spherical Zn crystals. Through a closer observation of a spherical crystal in the red frame, we found something curious. On the one hand, the left side of the selected spherical Zn crystal showed a morphology typical of Zn flakes (**Figure 2j**). These Zn flakes are almost the same size as those that were shown in **Figure 2g**. On the other hand, the top morphology of the selected spherical Zn crystal was flat and dense (**Figure 2k**). It seems that the upward growth of the Zn crystals was prevented by some external stress. The optical photograph embedded in **Figure 2h** shows the surface characteristics of the electrode after galvanizing.

In summary, we can extract two key points from the galvanizing tests. First, the deposited Zn crystals in the 2 M $ZnSO_4$ based aqueous electrolyte are generally micrometer-sized spheres. We tend to attribute this phenomenon to the high ionic conductivity and high $D_{(Zn^{2+})}$ of the aqueous $ZnSO_4$ electrolyte. The high ionic conductivity of the electrolyte could eliminate the $c_{(Zn^{2+})}$ gradient at the electrode surface, which will generate the spherical crystals.[50, 51] Second, the sluggish transport of Zn^{2+} in DNGF does not influence the spherical morphology of the electrodeposited Zn, but an external restriction could terminate their upward growth.

Based on our understanding that the surface tension is the mechanical force that contributes to the chemical potential change across the interface between the GPE and Zn crystals, the mechanical interaction can result in the change of exchange current density during the reaction of Zn plating/stripping because of the decrease in chemical potential difference (for the Zn deposition reaction): [33, 52, 53]

$$Zn^{2+} + 2e^- \longrightarrow Zn^0 \quad (\text{Plating}) \qquad \text{(Eq. 1)}$$

$$Zn^0 \longrightarrow Zn^{2+} + 2e^- \quad (\text{Stripping}) \qquad \text{(Eq. 2)}$$

The modified Butler-Volmer equation that describes the current-overpotential relationship can be written as:

$$j = j_0\left[\frac{c_{Zn^{2+}(surf)}}{c_{Zn^{2+}(bulk)}}\exp\left(-\frac{\beta F}{RT}\eta\right) - \frac{c_{Zn^0(surf)}}{c_{Zn^0(bulk)}}\exp\left(\frac{(1-\beta)F}{RT}\eta\right)\right] \quad (\text{Plating}) \qquad \text{(Eq. 3)}$$

where j is the local current density during Zn plating and j_0 is the exchange current density of Zn plating. β is the symmetry factor, and η is the overpotential of the electrode. It can be found from this equation that when j_0 decreases, the current density of galvanizing will also decrease.

In order to further verify the mechanical suppression effect of the DNGF on the formation of Zn dendrites, we conducted a potentiostatic Zn plating test. A Zn || Zn symmetric cell that was separated by GF or DNGF was firstly assembled. An Ag/AgCl reference electrode was connected to the as-assembled Zn || Zn cell to make a three-electrode Zn || Zn semi-solid-state cell (**Figure**

S6 in supporting information). The galvanizing tests were conducted under constant voltage and were stopped once the plating areal capacity achieved 40 mA h cm^{-2}. As shown in **Figure 3a**, when the plating potential was set as -1.05 V vs. Ag/AgCl, the corresponding current profile showed two stages during the plating process. In the first stage, the current density of Zn plating gradually increased to ~ 3 mA cm^{-2}. Then, at about 890 minutes, the current density of Zn plating began to decrease. This plating time was considered to be sufficient for the $c_{(Zn^{2+})}$ in the cell to achieve equilibrium. Therefore, we can attribute the decrease in current density to the decrease in j_0. The decrease in j_0 should come from the chemical potential reduction of the Zn plating reaction, because the expanded Zn crystals would induce better contact with the GPE framework during Zn deposition. As a comparison, the Zn || Zn cell without separator (**Figure 3a**, red line) showed a continuous increase in plating current density. After 490 minutes, the no-separator cell finally encountered a short circuit due to the unstoppable dendrite growth. Experiments under different plating potentials were employed to confirm our hypothesis. We found that in the DNGF GPE separated cells, when the capacity of Zn plating exceeded 30 mAh cm^{-2}, the current density did decrease, indicating that the mechanical suppression effect exists during Zn plating. Since the plating/stripping capacity was very high, the Zn foil on the stripping side inevitably underwent a huge morphological change (**Figure S7** in supporting information). The utilization of the three-electrode semi-solid-state cell ensured voltage stability during the tests (**Figure S8** in supporting information).

The observation of the topography of the electrodes further confirmed our hypothesis. As shown in **Figure 3b**, the Zn electrode after the potentiostatic plating at -1.13 V vs. Ag/AgCl exhibited a flat Zn coating with a thickness of about 200 μm. The Zn coating was observed to consist of spherical crystals instead of dendritic crystals (**Figure 3c**). The thickness of the Zn coating in the cases of plating at -1.05 V and -1.21 V were 110 μm and 240 μm, respectively (**Figure S9** and **Figure S10** in supporting information). The loose and thick Zn coating indicates that the deposition voltage of -1.21 V was too high, resulting in Zn crystals that could potentially break the gel framework. The top-view of the Zn electrode indicated that most of the spherical crystals would merge together to form a larger crystal aggregate structure with a flat surface (**Figure 3d** and **Figure 3e**). Optical photos of the as-tested samples gave intuitive information of the Zn plating process. As shown in **Figure 3f**, the Zn disk electrode that used DNGF as a separator had a uniform Zn coating on its surface, while the one without using a separator had several large Zn dendrites on its surface. Some Zn crystals grew into the gel matrix and were retained on the surface of the DNGF, which further confirmed the statement that the electrodeposited Zn crystals were in good contact with the GPE. We further used atomic force microscopy (AFM) to detect the morphology of the newly deposited Zn crystals on the two electrodes shown in **Figure 3f**. Dynamic force mode (DFM) was employed to measure the topography. As shown in **Figure 3g**, in the case of the DNGF separated cell, the newly deposited Zn crystal had a flat top surface with a global height difference of less than 40 nm. As a comparison, in the case of the no separator cell, the top surface is rough, and Zn flakes with a side length of around 0.5 μm were observed. At this point, we now have sufficient evidence to support our hypothesis that the growth of Zn dendrites can be inhibited by the mechanical suppression effect through the utilization of GPEs.

The mechanical suppression mechanism is discussed in **Figure 3i**. As depicted in the left part of **Figure 3i**, once the newly formed Zn nuclei appear on the substrate, Zn will grow along the preferential crystal orientation. Caused by the uneven distribution of the Zn^{2+} flux, the Zn crystals will grow in increasingly sharp peaks, which further induces the dendritic growth. Different from the free-growth mode, when a GPE framework is pressed onto the Zn plate, the Zn nuclei first deposit into the pores of the GPE framework and gradually ripen until achieving a size that can contact the polymer framework. Afterward, the further growth of Zn crystals applies strain to the GPE framework, so that the further growth of Zn crystals will experience higher stress from the GPE. Once the height of the Zn crystals reaches a level where the external stress is high enough to stop the Zn plating reaction, the upward growth tendency of the Zn crystals becomes suppressed. Subsequently, the as-formed Zn crystals will grow parallel to the surface, causing the individual spherical crystals to gather together to form a flat Zn coating layer. The mechanical suppression shown here is slightly different from the well-known mechanical suppression effect from solid-state electrolytes, the latter uses hard-enough materials (e. g. ceramics) to completely prevent upward growth of metals, and thus a controllable metal deposition can be achieved. Since the mechanical suppression reported by us uniformizes Zn deposition by reducing the upward growth tendency, so we call the mechanical suppression observed in our experiments “the modified mechanical suppression effect”, while the effective suppression of Zn dendrites growth can be achieved through the modified mechanical suppression effect.

To theoretically illustrate the modified mechanical suppression effect, we can gain insight from the modified Butler-Volmer equation:

$$j=j_0 \exp[\frac{(\beta_m - \beta)\Omega\sigma_{h,surf}}{RT}][\exp(\frac{(1-\beta)F\eta}{RT}) - \exp(\frac{(-\beta)F\eta}{RT})] \quad \text{(Eq. 4)}$$

where β_m is the mechanical cathodic symmetry factor, $\sigma_{h,surf}$ is the hydrostatic pressure on the interface and Ω is the partial molar volume[54, 55]. The inclusion of mechanical stress in the Butler-Volmer equation brings two effects: the rescaling of the exchange current density and the shift of the equilibrium potential. Increasing external stress results in the suppression of irregular Zn plating reactions. Moreover, the external stress helps to stop the unstable Zn ion transportation. [56, 57] Hence, the stable deposition can be achieved with the presence of mechanical restriction, which has also been confirmed by our direct observation of the Zn electrodes. It is worth mentioning that we also checked the in-plane XRD pattern of the Zn electrodes after the potentiostatic plating test (**Figure S11** in supporting information). However, the intensity in the [002] direction did not increase after Zn plating, indicating that the electroplated Zn was still polycrystalline.

Taking the additional mechanical stress into consideration will decrease the exchange current density and influence the deposition of Zn. We visualized the stress-affected Zn plating procedure by employing a Zn plating multi-field simulation based on the Butler-Volmer equation. **Figure 4a** shows the case when the initial nuclei

distribution is uneven, in which Zn deposition is not subject to external mechanical stress, namely, the free deposition mode. In this case, based on the mechanism of Zn dendritic growth and the observed Zn electrode as we mentioned above (**Figure 3f**), we assume that the deposition of Zn only occurs on the as-deposited spherical Zn nuclei. Here, the final height of the Zn coating is around 40 μm, and the observed overpotential during Zn plating is -30 mV (at a current density of 1 mA cm^{-2}). Slightly different from **Figure 4a**, in **Figure 4b**, the initial distribution of Zn nuclei is more uniform while the spherical Zn crystals are smaller than those in **Figure 4a**. The uniform initial distribution of Zn nuclei leads to a relatively low thickness of the Zn coating, which is around 34 μm. When the exchange current density is decreased to 5.72 A m^{-2} as obtained by linear sweep voltammetry (LSV) tests (**Figure S12**, **S13**, **S14** in supporting information), uniform deposition of Zn could be achieved (**Figure 4c**). The recorded plating overpotential as calculated by the Butler-Volmer equation is 80 mV, which is consistent with the data obtained in **Figure 2**. More specifically, the $c_{(Zn2+)}$ gradients near the electrode surface and across the whole cell are almost imperceivable (**Figure 4a-c**, right side), because of the ultra-high ionic conductivity of the 2 M $ZnSO_4$ aqueous electrolyte. The rapid transportation of Zn^{2+} can eliminate the concentration gradient, facilitate the uniform deposition of Zn, and help the formation of the spherical Zn crystals. This phenomenon is consistent with our previous observations. Geometric modeling of the Zn plating simulation can be found in the supporting information (**Figure S15**, supporting information). Moreover, when the current density was redistributed based on the geometric surface area, the distribution of the Zn coating can be further optimized (**Figure S16**, supporting information). The Zn plating behavior under the GPE is illustrated in **Figure 4d**. In agreement with our previous description, the upward growth tendency is suppressed by physical contact and the deposition of Zn will finally evolve into a flat coating with the presence of a mechanically strong GPE. At this point, we believe that it is possible to alleviate Zn dendrite growth through the modified mechanical suppression effect with a separator that possesses a shear modulus less than 1.8 times of the corresponding metal. Considering the thickness of the separator, the actual required modulus of the separator may be much smaller than this value. That is, it is possible to limit the growth of Zn dendrites by designing a polymer separator/electrolyte with proper mechanical strength.

2.3 Cyclic Zn plating/stripping performance of Zn || Zn symmetric cells.

Based on the understanding that DNGF can suppress the growth of Zn dendrites, and in order to detect the cyclic stability of the DNGF GPE and confirm the unique superiority of DNGF among various GPEs, we further assembled Zn || Zn symmetric cells that were separated by different GPEs. As shown in **Figure 5a**, Zn || Zn symmetric cells were tested at a constant current density of 1 mA cm^{-2} and a restricted areal capacity of 1 mAh cm^{-2}. PAM-GF, PAMPS-GF and glass fiber were used as control groups. First, the glass fiber separated Zn || Zn symmetric cell short-circuited after 48 cycles. As a reference, the PAM-GF separated cell could survive for nearly 100 cycles, while the PAMPS-GF separated cell worked for over 200 cycles. These control groups all short-circuited due to uncontrollable dendrite growth. The DNGF separated Zn || Zn symmetric cell could easily protect the cell from short-circuit for over 2500 h. The details of the voltage profiles for these Zn || Zn cells are shown in **Figure 5b**. During the initial 10-15 cycles, the DNGF separated cell showed a voltage hysteresis of around 180 mV, while the values for PAM-GF, PAMPS-GF or GF separated cell were 200 mV, 120 mV and 165 mV, respectively. The slightly higher overpotential for the DNGF separated cell indicates a slightly sluggish Zn^{2+} transportation in the DNGF framework. During the following 100-105 cycles, voltage hysteresis for the DNGF separated cell increased to about 210 mV and was stable for a long time. This could be attributed to the surface and volume change of the Zn electrodes, namely, the thickening of the Zn electrode. The change in electrode morphology led to contact between Zn and the GPE framework, indicated by the increase in the overpotential. During the 1000-1005 cycles, voltage hysteresis recovered to ~ 170 mV, due to the aggregation of deposited Zn crystals, as we have already emphasized in the above galvanizing experiments. The SEM observation helps confirm our conclusion, and a flat but polycrystalline surface of the as-cycled Zn electrode was shown in

(**Figure S17** supporting information). The thickness of the Zn electrode is about 210 μm, and no dendritic crystals were observed. As a comparison, by using PAM-GF and PAMPS-GF separators, Zn crystals damaged the GPE framework and produced large dendrites which pierced the GPE (**Figure S18**, **S19**, supporting information).

Considering that the measuring condition of 1mA cm^{-2}/ 1mAh cm^{-2} is far away from practical application values, the Zn || Zn symmetric cells were also tested under harsher conditions. Even when the current density was increased to 5 mA cm^{-2}, the DNGF separated Zn || Zn could maintain stable cyclic performance for over 1000 h, while the GF separated cell only worked for less than 100 h (**Figure S20**, supporting information). In addition to the superior dendrite suppressing capability of DNGF, we believe that the internal energy dissipation mechanism prevents the gel framework from being destroyed by Zn crystals during repeated Zn electroplating/stripping. This also helps to guarantee the long life-span of the DNGF separated cells.

2.4 Full cell test in Zn || MnO_2 battery under low capacity.

Encouraged by the superior Zn plating/stripping stability, we further conducted full cell tests by using a MnO_2 cathode, which could help us to further evaluate the potential of the DNGF-protected Zn metal anode for RAZIB applications. MnO_2 cathodes are considered excellent candidates for developing high energy density RAZIBs, due to their high theoretical capacity (308 mAh g^{-1} considering the 1 e^- transfers from Mn (IV) to Mn (III)) and high reduction potential.[13, 58-60] Here, 1D α-MnO_2 nanowires were fabricated through a hydrothermal method and were used as a cathode after being mixed with carbon black (**Figure S21**, supporting information). In most reports, in order to avoid the influence from the cathode architecture, Zn || MnO_2 cells have generally been tested by using MnO_2 cathodes with an areal mass loading of less than 2 mg cm^{-2}.[16, 61] Hence, we firstly tested the Zn || MnO_2 cells in such a condition. As shown in **Figure 5c**, the DNGF separated Zn || MnO_2 cell achieved an initial capacity of 161 mAh g^{-1} at a charge/discharge rate of 10 C (1C = 308 mA g^{-1}), and a capacity retention of 50% after

9500 cycles. At the same time, the GF separated cell unsurprisingly short-circuited in the end. **Figure 5d** highlights the changes in voltage profiles during cycling. It is clear that the discharging voltage plateau at around 1.35 V (vs. Zn/Zn^{2+}) gradually disappeared with increasing cycling. This phenomenon is a signal of decreasing particle-size, namely, the dissolution of MnO_2. [62] The dissolution and deposition of MnO_2 makes the energy storage mechanism of the Zn || MnO_2 cell gradually changed from a "battery" to a "pseudocapacitor". [62-65] By employing the model developed by Dunn and co-workers, we distinguished the quantitative capacitive contribution to the current response by cyclic voltammetry tests (CV). [66] As shown in **Figure 5e**, the capacitive contribution of the DNGF separated Zn || MnO_2 cell before cycling was 64.1% at a scan rate of 2 mV s^{-1}, and this value was increased to 91.0% after 9500 cycles. When the scan rate was increased to 5 mV s^{-1}, the capacitive contribution became more significant, which agreed with our conclusion. CV tests for the DNGF separated Zn || MnO_2 cell before cycling are shown in **Figure 5f**. The oxidation peaks shifted from 1.6 V to 1.75 V, indicating the oxidation of Mn species during charging could be processed normally when the cut-off voltage is set as 1.8 V. Moreover, the simulated capacitive current shows two oxidation peaks in **Figure 5g**, indicating that the oxidation peaks that we observed in the CV tests might come from two different reactions. For the GF separated Zn || MnO_2 cell, this phenomenon was also observed (**Figure S22**, supporting information). Benefiting from the decreasing particle size, the oxidation peaks shifted to the left after cycling (**Figure 5h**), proving the fact that the capacity decay for the DNGF separated Zn || MnO_2 cell is not caused by the increase in cell resistance. When comparing **Figure 5g** and **Figure 5i**, the current of the first oxidation peak decreased while the second oxidation increased after cycling, demonstrating the existence of changes to MnO_2 during cycling. All of this evidence points to a conclusion: some amount of MnO_2 undergoes a dissolution-deposition mechanism during charging/discharging, and as cycling progresses, the cathode becomes more and more like a pseudocapacitor rather than a battery under high current density.[64, 67-69] Consequently, the Zn || MnO_2 cell can readily achieve excellent cyclic performance at high charge/discharge rates, as we demonstrated before. Obviously, we should note carefully that the cyclic performance of the Zn || MnO_2 batteries in this case cannot represent the practical performance of the studied Zn || MnO_2 batteries. Moreover, we also assembled Zn || MnO_2 cells with different kinds of MnO_2 and various MnO_2 loadings. The observed capacity of the DNGF separated Zn || MnO_2 cell is generally lower than the GF separated Zn || MnO_2 cell due to the sluggish ion transport (**Figure S23**, supporting information), but considering that all of the GF separated Zn || MnO_2 cells ultimately short-circuited, GF is not a practical material for separating RAZIBs.

2.5 Full cell test of Zn || MnO_2 batteries under high-capacity.

In order to provide valid information for the development of RAZIBs with high energy density, we tried to assemble high-capacity Zn || MnO_2 cells by using MnO_2 cathodes with ultra-high areal capacity. This is required because the cathode capacity, which is equivalent the anode value, is necessary for the battery to achieve a high energy density. As shown in **Figure S24** (supporting information), the MnO_2 cathode with an MnO_2 mass loading of 30 mg cm^{-2} (theoretical areal capacity: 9.2 mAh cm^{-2}) was prepared and referred to as the high-capacity MnO_2 cathode (HCM cathode). The HCM cathodes were used in Zn || MnO_2 cells that were separated by DNGF or GF. As shown in **Figure 6a**, the specific capacity of the DNGF separated high-capacity Zn || MnO_2 cell decreased rapidly with increasing charge/discharge rate. The discharge capacities at 0.1 C and 0.3 C were 290 mAh g^{-1} and 180 mAh g^{-1}. When the discharge rate was increased to 1 C, the Zn || MnO_2 cell with DNGF showed an initial capacity of 160 mAh g^{-1}. Then the capacity gradually decreased to 60 mAh g^{-1} with cycling (**Figure 6b**). No short-circuit was observed for the DNGF separated Zn || MnO_2 cell, while the GF separated cell short-circuited after just 29 cycles. This implies that the most significant issue in RAZIBs, dendrite growth, can be solved by using a DNGF GPE. Voltage profiles at the 5th cycle, 50th cycle, 250th cycle and 500th cycle maintained clear discharge plateaus at around 1.2 V, indicating that the Zn || MnO_2 cell was still a "battery" during cycling (**Figure 6c**). This phenomenon implies that the reason for capacity decay of the high-capacity cell may be different from the low-capacity one.

A galvanostatic intermittent titration technique (GITT) was conducted to detect the reason for the capacity decay. By adding rest intervals to separate the discharge processes, ions have enough diffusion time, so that the mass transfer resistance can be alleviated during the GITT test.[70] **Figure 6d** shows the discharge behavior of the Zn || MnO_2 cell after 500 cycles. It can be clearly seen that the capacity of the cell had returned to 160 mAh g^{-1} during the GITT test, so that the capacity difference between the GITT cycle and the normal cycle of the as-cycled HCM electrode is about 100 mAh g^{-1}. As a comparison, the newly prepared HCM electrode, which showed a discharge capacity of around 252 mAh g^{-1} during the GITT cycle, also exhibited the difference in capacity between the direct galvanostatic charge/discharge mode and the GITT mode is about 100 mAh g^{-1}.**(Figure S25**) These two close values indicate that the HCM electrode undergone an irreversible loss of capacity during the cycle. Therefore, we believe that the fading in capacity of the HCM cathode can be attributed to two aspects: 1) α -MnO_2 gradually loses its activity during charging and discharging, which is the main reason of the irreversible capacity; 2) the poor electrode architecture causes the electrolyte inside the electrode to be quickly depleted and cannot be replenished, which in turn causes the electrode reactions can only occur on the surface. This part of the capacity loss can be recovered after the electrolyte is replenished to the inside of the HCM electrode, but when the gel electrolyte is used or the charge/discharge rate is fast, the discharge capacity will quickly decay due to the high mass transfer resistance caused by poor ion diffusion. Based on the conclusions from Sun et al., we can define two regions in the GITT test, related to Zn^{2+} intercalation and H^+ intercalation.[71] In GITT, the voltage jump immediately after applying current could be attributed to the ohmic impedance and charge transfer resistance. Therefore, the large overvoltage for the Zn^{2+} intercalation reaction can be explained by the slow ion diffusion. By comparing the electrochemical impedance spectra (EIS) before and after cycling, we found that the charge transfer resistance decreased after cycling, while ohmic resistance increased slightly (**Figure S26**, supporting information). CV tests confirmed our idea from the electrochemical aspect. The oxidation peak at around 1.6 V in **Figure 6e** gradually disappeared with increasing scan rate. This shows that the huge overvoltage prevented the electrode reactions from proceeding. With the depletion of electrolyte inside the cathode framework, this phenomenon would become more serious as the electrochemical cycling progresses (**Figure 6f**). The

geometrically normalized capacitive contribution ratio of the as-cycled Zn || MnO_2 cell is shown in **Figure 6g**. The capacitive current ratio of the cell before cycling was only about 27% at low scanning speed, and this value barely changed during cycling, indicating that the high-capacity Zn-MnO_2 cell maintained the same discharge characteristics during low-rate charging/discharging. However, the ratio of capacitive current increased rapidly as the scanning speed increased. One possible reason for this phenomenon might be the electrode reaction could only proceed on the surface of the cathode when the charge/discharge rate was very high. The electrolyte inside the cathode becomes depleted quickly at a high charge/discharge rate, and thus the further continuation of electrode reactions inside the cathode would be more difficult. However, the electrochemical process of the high-capacity Zn || MnO_2 cell during high-rate charge/discharge is very complicated and nonuniform, which makes it impossible to accurately predict the capacitor/battery characteristics of the material by using Dunn's model (**Figure S27**, supporting information). This is also the reason why the percentage of the capacitive current observed at high scan rate exceeded 100%, which is obviously unrealistic. It is worth mentioning that the problem of cathode architecture was also observed in the GF separated high-capacity Zn || MnO_2 cell, indicating that the hindrance of the electrode reactions did not come from the relatively low ion conductivity of DNGF (**Figure S28**, supporting information).

Characterization of the HCM cathode before and after cycling is shown in **Figure 7**. The HCM cathode was removed from the DNGF separated Zn || MnO_2 cell that had undergone 500 cycles (corresponding to **Figure 6**). As exhibited in **Figure 7a**, the HCM cathode before cycling shows a modified XRD pattern of α-MnO_2. During the first 500 cycles, the following reactions were processed:[72]

$$MnO_2 + H_2O + e^- \longrightarrow MnOOH + OH^- \quad \text{(Eq. 5)}$$

$$yZn^{2+} + MnO_2 \cdot xH_2O + 2ye^- \longrightarrow Zn_yMnO_2 \cdot xH_2O \quad \text{(Eq. 6)}$$

$$Zn^{2+} + 6OH^- + SO_4^{2-} + 5H_2O \rightleftharpoons Zn_4(OH)_6SO_4 \cdot 5H_2O\downarrow \quad \text{(Eq. 7)}$$

Therefore, peaks indicating $ZnMn_2O_4$, $Zn_4(OH)_6SO_4$ and MnOOH were observed after cycling. An additional galvanostatic discharge measurement was conducted after reassembling the DNGF separated high-capacity Zn || MnO_2 cell. The HCM cathode was soaking in electrolyte (2M $ZnSO_4$ + 0.2 M $MnSO_4$) for 12 h before the test. The reassembled high-capacity Zn || MnO_2 cell surprisingly provided a capacity of 140 mAh g^{-1} (calculated by the HCM cathode), indicating that the electrochemical capacity, which was not utilized due to the poor architecture of the HCM cathode, could be reactivated after the infiltration of the electrolyte (**Figure 7b**). In-situ Raman spectroscopy during the additional discharge test (corresponding to **Figure 7b**) was also conducted. As shown in **Figure 7c**, in the discharge region of point 8 - point 23, the intensity of $ZnMn_2O_4$ and MnOOH increased slightly as the discharge proceeded. Energy-dispersive X-ray spectroscopy (EDS) was employed to compare the compositional differences of the HCM cathode before and after cycling. As shown in **Figure 7d**, before cycling, the HCM cathode showed a carbon substrate that was covered by MnO_2 nanowires. While in **Figure 7e**, the as-cycled HCM cathode exhibited a surface that was covered by shapeless nanoparticles consisting of Zn, Mn and O atoms. The change in morphology of the MnO_2 nanowires should be the result of the phase transition caused by the intercalation reaction, which possibly caused the irreversible capacity decay. Based on the analysis above, we believe that the main problem of utilizing the HCM cathode comes from two aspects: the poor electrode architecture that inhibits the effective utilization of MnO_2, and the change in active materials that causes an irreversible damage.

3. Experimental methods

3.1 Preparation of the hydrogel polymer framework. To prepare the PAMPS-GF hydrogel, 1 M AMPS (Toagosei Co. Ltd.) was dissolved in DI water. Then, 2.5 % (mole ratio) MBAA (FUJIFILM Wako Pure Chemical Corporation) and 1 % (mole ratio) α-keto (FUJIFILM Wako Pure Chemical Corporation) were added to the solution. The AMPS solution was then transferred to an argon (Ar) filled glovebox. A piece of glass fiber filter (Advantec. GA-100) was cut to a size of 10 cm x 10 cm and soaked in the as-prepared AMPS solution for 30 minutes. Afterward, the glass fiber sheet was sandwiched between two glass plates, and was exposed to UV light for 12 h.

The obtained PAMPS-GF composite was soaked in a 3M acrylamide (AM, Junsei Chemical) solution for 1 day, in order to thoroughly swell the PAMPS-GF skeleton with AM solution. 0.01 % MBAA and 0.01 % α-keto were also added to the AM solution. The AM-swollen PAMPS-GF was transferred to a glovebox and was polymerized by a 12 h UV irradiation.

To prepare the PAM-GF and PAM, the aforementioned AM solution was used to infiltrate a glass fiber sheet. PAM-GF can be obtained by polymerizing the AM-filled glass fiber while PAM was prepared by polymerizing the AM solution in a glass mold.

All the obtained hydrogel samples were kept in DI water until use.

3.2 Galvanostatic Zn plating/stripping tests. All the DNGF samples that were used in the Zn plating tests were firstly dried in a vacuum box at room temperature for 48 h and then soaked in a 2 M $ZnSO_4$ aqueous solution (as electrolyte) for 24 h. Electrolyte dosage for every GF separated cell was 200 μL. For the galvanostatic galvanizing tests, Swagelok Zn || Zn cells that were separated by DNGF or GF were assembled and connected to a battery tester (HJ1020SD8 Hokuto Denko). Zn metal was electroplated to a piece of Zn disk electrode at a constant current density of 1 mA cm^{-2} for 16 h. For the potentiostatic Zn plating tests, homemade three-electrode cells were assembled as shown in **Figure S6**. Two Zn disk

electrodes were used as a working electrode and a counter electrode, respectively. An Ag/AgCl reference electrode was inserted into the window that was opened on the body of the Swagelok cell. Additional 200 µL electrolyte (2 M $ZnSO_4$) was added to the cell in order to achieve the contact between the reference electrode and electrolyte. Zn metal was electroplated at a constant potential as demonstrated in the context. The experiments were stopped manually once the areal capacity of Zn plating met the specific value. For the Zn || Zn symmetric cell tests, two-electrode Swagelok cells with two Zn disk electrodes were prepared. DNGF, PAM-GF, PAMPS-GF and GF were used to separate the cells. All the GPE samples that were used in the symmetric cell tests were firstly dried in a vacuum box at room temperature for 48 h and then soaked in a 2 M $ZnSO_4$ aqueous solution for 24 h. Electrolyte dosage for every GF separated cell was 200 µL. Zn || Zn symmetric cells were tested on the SD8 battery tester. During the test, Zn metal plating/stripping between two Zn electrodes at a constant current density was repeated.

3.3 Test of Zn || MnO_2 cells. The α-MnO_2 nanowires were prepared through a one-step hydrothermal method. $MnSO_4$ ($MnSO_4 \cdot 5H_2O$, Kanto Chemical Co., Inc., 99.0%) and $KMnO_4$ (Wako Chem. 99.3%) were dissolved in DI water with a molar ratio of 5:2. The obtained solution was stirred in air for 1 h and then transferred to a Teflon container. The hydrothermal reaction took 12 h at 140 ℃. After filtration, the obtained dark brown residue was washed by DI water and ethanol several times. Finally, the dark brown powder was dried in a vacuum oven at 80℃ for 12h. The used electrolytic manganese dioxide (EMD, TOSOH, HH-TF 40µm) was obtained from TOSOH company. MnO_2 cathodes were prepared by mixing 65 wt% MnO_2 powder, 25 wt% carbon black (ketjen black, KB), and 10 wt% poly(tetrafluoroethylene) (PTFE, suspension, 10 wt%) in ethanol aqueous solution. The amount of active material was controlled by adjusting the thickness of the cathode. The freestanding electrode was prepared by pressing the carbon-MnO_2 mixture onto a titanium (Ti) mesh (Nilaco, 100 mesh).

The low-capacity MnO_2 cathode was prepared by mixing 65 wt% MnO_2 powder, 25 wt% carbon black (ketjen black, KB), and 10 wt% poly(vinylidene fluoride) (PVDF, powder) in N,N-Dimethylformamide (DMF). The mixture was then coated onto a Ti mesh and dried in a vacuum oven at room temperature overnight.

Zn || MnO_2 cells were assembled by using Zn metal anodes and different MnO_2 cathodes. Swagelok cells were used as the cell casing and DNGF or GF was used as the separator. All the DNGF samples that were used in the Zn || MnO_2 cell tests were firstly dried in a vacuum box at room temperature for 48 h and then soaked in an aqueous solution containing 2 M $ZnSO_4$ and 0.2 M $MnSO_4$ for 24 h. The electrolyte dosage for every GF separated cell was 200 µL. The Zn || MnO_2 cells were charged/discharged between 0.8 V and 1.8 V at specific current densities.

3.4 Characterization. X-ray diffraction (XRD) patterns were obtained by using an X-ray diffractometer (Rigaku MiniFlex600) using Cu Ka radiation.

Scanning electron microscope (SEM) observations and energy dispersive spectroscopy (EDS) measurements were conducted on an SEM (ZEISS Sigma 500). Atomic force microscopy (AFM) tests were conducted on an AFM (Hitachi, NanonaviSII) by using the dynamic force mode (DFM).

In-situ Raman spectra was recorded by a Raman microscope (RENISHAW Raman spectrometer) using an excitation wavelength of 532 nm.

Before the ex-situ SEM observation of GPEs framework and as-tested Zn electrodes, all samples were soaked in sufficient DI water for 1 day after they were taken out from the cells, in order to remove residue of electrolytes. Afterwards, all the samples were freeze-dried and kept in a vacuum box before observation.

Additional experimental details can be found in the supporting information.

4. Conclusions

In summary, we achieved a dendrite-free Zn metal anode by using a novel high strength DNGF gel polymer electrolyte. Thanks to the modified mechanical suppression effect, the dendrite-free Zn || Zn symmetric cell could survive for over 1000 h, even at a high current density of 5 mA cm^{-2}. Some interesting phenomena related to the deposition of Zn with GPEs were observed, and the modified mechanical suppression effect for preventing Zn dendrite growth was discussed. Firstly, when Zn was deposited under a GPE framework (e.g. DNGF), the deposition initially occurred in the pores of the porous GPE, due to the lack of external stress inside the pores. The uniform pore distribution on the GPE surface ensured a uniform initial deposition of Zn. Secondly, the upward growth of Zn crystals could be restricted when they were contacting the GPE framework. Once the upward growth of Zn crystals was stopped, Zn crystals would grow parallel to form a flat surface. Hence, the pore-size and mechanical strength of the GPE determines the maximum height of the Zn crystal. Thirdly, the mechanical suppression of dendrite growth occurred at the expense of increasing the deposition overpotential. A reasonable design of the GPE pore-size distribution would make it possible to reduce the thickness of the GPE and overpotential of Zn deposition simultaneously. Similar ideas can be employed for designing porous separators to suppress dendrite growth with different metal anodes, like we depicted in **Figure S29**-**Figure S31** (supporting information).

Finally, a high-capacity and long-life Zn || MnO_2 rechargeable battery was achieved by using the DNGF GPE. The Zn || MnO_2 battery was stable for over 500 cycles and showed a capacity retention of 40%. This indicates that short-circuiting, the weakness most often shown in RAZIBs, can be solved by using the high strength DNGF GPE. Moreover, we further studied the capacity decay mechanism of the high-capacity Zn || MnO_2 battery, and two crucial conclusions were discovered: firstly, it is irrational to use the performance of low-capacity MnO_2 cathodes during high-rate

charge/discharge as a real performance evaluation, because low-capacity MnO_2 cathodes exhibit obvious capacitor-characteristics during high-rate charge/discharge. This might be an important reason why previously reported Zn || MnO_2 batteries that were tested with low-capacity cathodes and high charge/discharge rates showed superior cyclic performance. Secondly, we think that poor cathode architecture (thick, high tortuosity) is the main contributing factor of capacity decay in high-capacity Zn || MnO_2 batteries. The changes to the cathode materials over 500 cycles does not lead to a significant capacity degradation of the battery. This could be seen by the fact that even after the cathode material has undergone significant changes in morphology and composition, the capacity of the cathode can still be maintained. This indicates that to develop high energy density Zn || MnO_2 batteries, the structural design of a high-capacity cathode will be an important subject in the future.

In this work we outline the important criteria for developing GPEs that can suppress Zn dendrite growth and demonstrate their necessity towards achieving high-energy-density RAZIBs. Furthermore, we believe this work could pave the way for the development of flexible and wearable electronics based on RAZIBs.

Author Contributions

D. R. King and C. Zhu conceived the idea for this study and supervised the work. D. R. King, C. Zhu and R. Zhu designed the experiments. W. Cui and R. Zhu prepared the samples used in this work and did the characterization. R. Zhu, Z. Xiong, C. Tang and H. Yang performed electrochemistry characterizations. T. Huang, L. Fadillah and R. Zhu performed the simulation. R. Zhu wrote the original the manuscript. D. Kowalski, S. Kitano, Y. Aoki, T. Kurokawa, H. Habazaki, C. Zhu and D. R. King revised the manuscript. All authors commented on the final manuscript.

Conflicts of interest

There are no conflicts to declare.

Acknowledgements

This work was supported partially by the Japan Society for Promotion of Science (JSPS). A part of the characterization work was conducted at Hokkaido University, supported by the "Nanotechnology Platform" Program of the Ministry of Education, Culture, Sports, Science and Technology (MEXT), Japan. R. Zhu would like to thank the support by the Program for Leading Graduate Schools (Hokkaido University "Ambitious Leader's Program") and Grant-in-Aid for JSPS Research Fellow. C. Zhu also acknowledges the support from the National Natural Science Foundation of China (No. 52006238), the Natural Science Foundation of Jiangsu Province (No. BK20200635) and the Fundamental Research Funds for the Central University (grant no. 2020ZDPYMS24). D. R. King would like to acknowledge funding from JSPS Grant-in-Aid for Scientific Research Nos. 17H06144 and 20K20193. The authors thank the members of Prof. Jian Ping Gong's laboratory for helping with the experiments.

Notes and references

1. Y. P. Deng, R. L. Liang, G. P. Jiang, Y. Jiang, A. P. Yu and Z. W. Chen, *ACS Energy Letters*, 2020, **5**, 1665-1675.

2. G. Z. Fang, J. Zhou, A. Q. Pan and S. Q. Liang, *ACS Energy Letters*, 2018, **3**, 2480-2501.

3. J. Liu, Z. Bao, Y. Cui, E. J. Dufek, J. B. Goodenough, P. Khalifah, Q. Li, B. Y. Liaw, P. Liu, A. Manthiram, Y. S. Meng, V. R. Subramanian, M. F. Toney, V. V. Viswanathan, M. S. Whittingham, J. Xiao, W. Xu, J. Yang, X.-Q. Yang and J.-G. Zhang, *Nature Energy*, 2019, **4**, 180-186.

4. C. Fang, X. Wang and Y. S. Meng, *Trends in Chemistry*, 2019, **1**, 152-158.

5. Q. Zhang, J. Luan, Y. Tang, X. Ji and H. Wang, *Angew. Chem. Int. Ed.*, 2020, **59**, 13180-13191.

6. L. Kang, M. Cui, F. Jiang, Y. Gao, H. Luo, J. Liu, W. Liang and C. Zhi, *Advanced Energy Materials*, 2018, **8**, 1801090.

7. H. Yang, Z. Chang, Y. Qiao, H. Deng, X. Mu, P. He and H. Zhou, *Angew. Chem. Int. Ed.*, 2020, **59**, 9377-9381.

8. T. M. Gür, *Energy & Environmental Science*, 2018, **11**, 2696-2767.

9. Q. Yang, G. Liang, Y. Guo, Z. Liu, B. Yan, D. Wang, Z. Huang, X. Li, J. Fan and C. Zhi, *Adv. Mater.*, 2019, **31**, e1903778.

10. J. Fu, R. Liang, G. Liu, A. Yu, Z. Bai, L. Yang and Z. Chen, *Adv. Mater.*, 2019, **31**, e1805230.

11. D. H. Wang, C. P. Han, F. N. Mo, Q. Yang, Y. W. Zhao, Q. Li, G. J. Liang, B. B. Dong and C. Y. Zhi, *Energy Storage Materials*, 2020, **28**, 264-292.

12. X. Wang, F. Wang, L. Wang, M. Li, Y. Wang, B. Chen, Y. Zhu, L. Fu, L. Zha, L. Zhang, Y. Wu and W. Huang, *Adv. Mater.*, 2016, **28**, 4904-4911.

13. D. Chao, W. Zhou, C. Ye, Q. Zhang, Y. Chen, L. Gu, K. Davey and S. Z. Qiao, *Angew. Chem. Int. Ed.*, 2019, **58**, 7823-7828.

14. Z. Guo, Y. Ma, X. Dong, J. Huang, Y. Wang and Y. Xia, *Angew. Chem. Int. Ed.*, 2018, **57**, 11737-11741.

15. J. Zhao, K. K. Sonigara, J. Li, J. Zhang, B. Chen, J. Zhang, S. S. Soni, X. Zhou, G. Cui and L. Chen, *Angew. Chem. Int. Ed.*, 2017, **56**, 7871-7875.

16. F. Mo, G. Liang, Q. Meng, Z. Liu, H. Li, J. Fan and C. Zhi, *Energy & Environmental Science*, 2019, **12**, 706-715.

17. Y. Huang, J. Y. Zhang, J. W. Liu, Z. X. Li, S. Y. Jin, Z. G. Li, S. D. Zhang and H. Zhou, *Materials Today Energy*, 2019, **14**, 100349.

18. N. Sun, F. Lu, Y. Yu, L. Su, X. Gao and L. Zheng, *ACS Appl. Mater. Interfaces*, 2020, **12**, 11778-11788.

19. X.-B. Cheng and Q. Zhang, *Journal of Materials Chemistry A*, 2015, **3**, 7207-7209.

20.H. J. S. Sand, *The London, Edinburgh, and Dublin Philosophical Magazine and Journal of Science*, 2010, **1**, 45-79.

21. Y. Zeng, X. Zhang, R. Qin, X. Liu, P. Fang, D. Zheng, Y. Tong and X. Lu, *Adv. Mater.*, 2019, **31**, e1903675.

22. C. Li, Z. Sun, T. Yang, L. Yu, N. Wei, Z. Tian, J. Cai, J. Lv, Y. Shao, M. H. Rummeli, J. Sun and Z. Liu, *Adv. Mater.*, 2020, **32**, e2003425.

23. J. S. Ko, A. B. Geltmacher, B. J. Hopkins, D. R. Rolison, J. W. Long and J. F. Parker, *ACS Applied Energy Materials*, 2018, **2**, 212-216.

24. J. F. Parker, E. S. Nelson, M. D. Wattendorf, C. N. Chervin, J. W. Long and D. R. Rolison, *ACS Appl. Mater. Interfaces*, 2014, **6**, 19471-19476.

25. Z. Kang, C. L. Wu, L. B. Dong, W. B. Liu, J. Mou, J. W. Zhang, Z. W. Chang, B. Z. Jiang, G. X. Wang, F. Y. Kang and C. J. Xu, *ACS Sustainable Chemistry & Engineering*, 2019, **7**, 3364.

26. J. Zheng, Q. Zhao, T. Tang, J. Yin, C. D. Quilty, G. D. Renderos, X. Liu, Y. Deng, L. Wang, D. C. Bock, C. Jaye, D. Zhang, E. S. Takeuchi, K. J. Takeuchi, A. C. Marschilok and L. A. Archer, *Science*, 2019, **366**, 645-648.

27. Y. Yin, S. Wang, Q. Zhang, Y. Song, N. Chang, Y. Pan, H. Zhang and X. Li, *Adv. Mater.*, 2019, **32**, 1906803.

28. T. Foroozan, V. Yurkiv, S. Sharifi-Asl, R. Rojaee, F. Mashayek and R. Shahbazian-Yassar, *ACS Appl. Mater. Interfaces*, 2019, **11**, 44077-44089.

29. K. Yan, Z. Lu, H.-W. Lee, F. Xiong, P.-C. Hsu, Y. Li, J. Zhao, S. Chu and Y. Cui, *Nature Energy*, 2016, **1**, 16010.

30. T. Krauskopf, F. H. Richter, W. G. Zeier and J. Janek, *Chem. Rev.*, 2020, **120**, 7745-7794.

31. Y. Takeda, O. Yamamoto and N. Imanishi, *Electrochemistry*, 2016, **84**, 210-218.

32. C. Yang, K. Fu, Y. Zhang, E. Hitz and L. Hu, *Adv. Mater.*, 2017, **29**, 1701169.

33. Z. Hong, Z. Ahmad and V. Viswanathan, *ACS Energy Letters*, 2020, **5**, 2466-2474.

34. C. Monroe and J. Newman, *Journal of The Electrochemical Society*, 2004, **151**, 880-886.

35. X. Zhang, A. Wang, X. Liu and J. Luo, *Acc. Chem. Res.*, 2019, **52**, 3223-3232.

36. J. P. Gong, *Soft Matter*, 2010, **6**, 2583.

37. T. Nakajima, H. Furukawa, Y. Tanaka, T. Kurokawa, Y. Osada and J. P. Gong, *Macromolecules*, 2009, **42**, 2184-2189.

38. J. P. Gong, Y. Katsuyama, T. Kurokawa and Y. Osada, *Adv. Mater.*, 2003, **15**, 1155-1158.

39. Y. Lu, T. Zhu, N. Xu and K. Huang, *ACS Applied Energy Materials*, 2019, **2**, 6904-6910.

40. D. Chao, C. R. Zhu, M. Song, P. Liang, X. Zhang, N. H. Tiep, H. Zhao, J. Wang, R. Wang, H. Zhang and H. J. Fan, *Adv. Mater.*, 2018, **30**, e1803181.

41. D. A. Cogswell, *Phys. Rev. E.*, 2015, **92**, 011301.

42. Y. Zhang, Y. Zhong, Q. Shi, S. Liang and H. Wang, *The Journal of Physical Chemistry C*, 2018, **122**, 21462-21467.

43. D. R. Ely, A. Jana and R. E. García, *Journal of Power Sources*, 2014, **272**, 581-594.

44. A. Jana and R. E. García, *Nano Energy*, 2017, **41**, 552-565.

45. X. Ren, S. Chen, H. Lee, D. Mei, M. H. Engelhard, S. D. Burton, W. Zhao, J. Zheng, Q. Li, M. S. Ding, M. Schroeder, J. Alvarado, K. Xu, Y. S. Meng, J. Liu, J.-G. Zhang and W. Xu, *Chem*, 2018, **4**, 1877-1892.

46. H. Zhang, G. G. Eshetu, X. Judez, C. Li, L. M. Rodriguez-Martinez and M. Armand, *Angew. Chem. Int. Ed.*, 2018, **57**, 15002-15027.

47. K. Xu, *Chem. Rev.*, 2004, **104**, 4303-4417.

48. J. Cao, D. Zhang, X. Zhang, M. Sawangphruk, J. Qin and R. Liu, *Journal of Materials Chemistry A*, 2020, **8**, 9331-9344.

49. J. Shin, J. Lee, Y. Park and J. W. Choi, *Chem. Sci.*, 2020, **11**, 2028-2044.

50. F. Yang, *Phys. Chem. Chem. Phys.*, 2020, **22**, 13737-13745.

51. Y. Wang, Z. Wang, D. Lei, W. Lv, Q. Zhao, B. Ni, Y. Liu, B. Li, F. Kang and Y. B. He, *ACS Appl. Mater. Interfaces*, 2018, **10**, 20244-20249.

52. C. Monroe and J. Newman, *Journal of The Electrochemical Society*, 2005, **152**, A396-404.

53. J. K. Nørskov, T. Bligaard, A. Logadottir, J. R. Kitchin, J. G. Chen, S. Pandelov and U. Stimming, *Journal of The Electrochemical Society*, 2005, **152**, J23-26.

54. V. Yurkiv, T. Foroozan, A. Ramasubramanian, M. Ragone, R. Shahbazian-Yassar and F. Mashayek, *Journal of The Electrochemical Society*, 2020, **167**.

55. B. Wu and W. Lu, *Journal of the Mechanics and Physics of Solids*, 2019, **125**, 89-111.

56. Z. Ahmad and V. Viswanathan, *Phys. Rev. Lett.*, 2017, **119**, 056003.

57. Z. Ahmad and V. Viswanathan, *Phys. Rev. Mater.*, 2017, **1**, 055403.

58. Y. Jiang, D. Ba, Y. Li and J. Liu, *Adv. Sci.*, 2020, **7**, 1902795.

59. M. Mateos, N. Makivic, Y. S. Kim, B. Limoges and V. Balland, *Advanced Energy Materials*, 2020, **10**, 2000332.

60. Y. Jiang, D. Ba, Y. Li and J. Liu, *Advanced Science*, 2020, **7**, 1902795.

61. D. Wang, L. Wang, G. Liang, H. Li, Z. Liu, Z. Tang, J. Liang and C. Zhi, *ACS Nano*, 2019, **13**, 10643-10652.

62. V. Augustyn, P. Simon and B. Dunn, *Energy & Environmental Science*, 2014, **7**, 1597.

63. L. Wang, X. T. Wang, J. H. Zhong, K. Xiao, T. Ouyang and Z. Q. Liu, *Chemistry*, 2021, **27**, 1.

64. G. Liang, F. Mo, H. Li, Z. Tang, Z. Liu, D. Wang, Q. Yang, L. Ma and C. Zhi, *Advanced Energy Materials*, 2019, **9**, 1901838.

65. J. K. Seo, J. Shin, H. Chung, P. Y. Meng, X. Wang and Y. S. Meng, *The Journal of Physical Chemistry C*, 2018, **122**, 11177-11185.

66. J. Wang, J. Polleux, J. Lim and B. Dunn, *The Journal of Physical Chemistry C*, 2007, **111**, 14925-14931.

67. P. Simon, Y. Gogotsi and B. Dunn, *Science*, 2014, **343**, 1210-1211.

68. V. Augustyn, J. Come, M. A. Lowe, J. W. Kim, P. L. Taberna, S. H. Tolbert, H. D. Abruna, P. Simon and B. Dunn, *Nat. Mater.*, 2013, **12**, 518-522.

69. H. Chen, S. Cai, Y. Wu, W. Wang, M. Xu and S. J. Bao, *Materials Today Energy*, 2021, **20**, 100646.

70. Y. Zhu and C. Wang, *Journal of Physical chemistry C*, 2010, **6**, 2830-2841.

71. W. Sun, F. Wang, S. Hou, C. Yang, X. Fan, Z. Ma, T. Gao, F. Han, R. Hu, M. Zhu and C. Wang, *J. Am. Chem. Soc.*, 2017, **139**, 9775-9778.

72. X. Jia, C. Liu, Z. G. Neale, J. Yang and G. Cao, *Chem. Rev.*, 2020, **120**, 7795-7866.

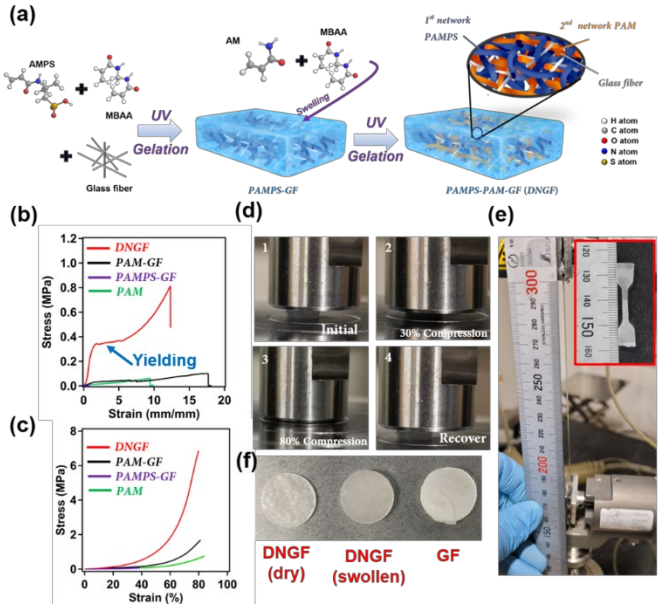

Figure. 1 Preparation and characterization of the DNGF. (a) Scheme for the fabrication of the DNGF gel matrix. Loading curves of different gels under (b) uniaxial elongation and (c) uniaxial compression. (d) Photographs demonstrating the DNGF sustaining high compression. (e) Photographs demonstrating the stretchability of the DNGF. The inset photo is the dumbbell-shaped DNGF sample before the test. (f) Photographs of DNGF and GF.

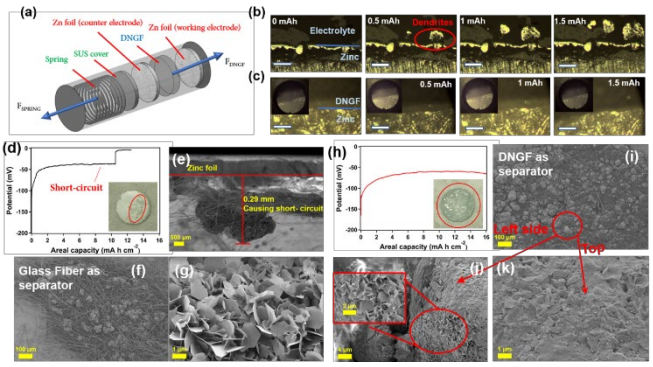

Figure. 2 Galvanostatic electrodeposition behavior of Zn under different conditions. (a) Configuration of the measurement cell. In-situ optical observations for the deposition of Zn (b) without the use of a separator and (c) using DNGF as the separator. The scale bar is 100 μm, while the insets are the panorama of the observation window under the optical microscope, the circular window comes from a 1 mm diameter observation window. (d) Voltage profile during galvanization with the use of a glass fiber separator, and the inset optical photo is the corresponding Zn electrode. (e,f,g) SEM images of glass fiber separated Zn electrode after electroplating. (h) Voltage profile during galvanizing with the use of a DNGF GPE, and the inset optical photo is the corresponding Zn electrode. (i,j,k) SEM images of DNGF separated Zn electrode after electroplating.

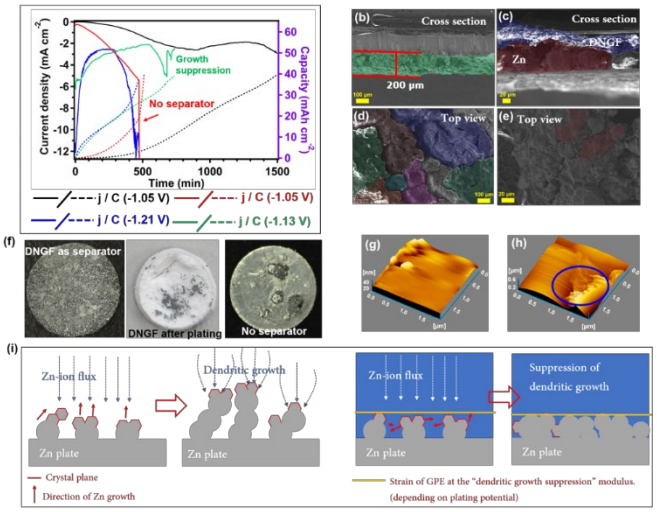

Figure. 3 Potentiostatic electrodeposition behavior of Zn under different conditions. (a) current profiles of Zn deposition using DNGF at a constant voltage of -1.05 V (black solid line), -1.13 V (green solid line), and -1.21 V (blue solid line) vs. Ag/AgCl. The red solid line refers to the no-separator cell, and the dotted lines are the corresponding capacity profiles. (b,c) Cross-sectional and (d,e) top-view SEM images of the Zn electrodes after Zn deposition at a constant voltage of -1.13 V vs. Ag/AgCl. (f) Optical photos of the Zn electrode (left) and DNGF (mid) after Zn deposition at a constant voltage of -1.13 V vs. Ag/AgCl. The photo on the right side is the Zn electrode in the cell without separator. DFM detection of (g) the Zn electrode after Zn deposition at a constant voltage of -1.13 V vs. Ag/AgCl and (h) the Zn electrode in the no-separator cell. (i) Schematic illustration explaining the dendrite suppression behavior.

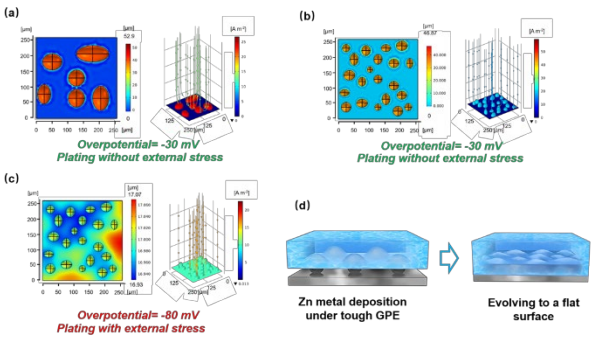

Figure. 4 Simulated results of the thickness change during Zn plating under different conditions. (a,b) Growth of Zn during galvanostatic plating in a no-separator cell (left), and the corresponding current field is shown in the right side. (c) Growth of Zn during galvanostatic plating in a cell with DNGF separator (left), and the corresponding current field is shown on the right side. (d) Schematic illustration of Zn growth behavior under the high strength hydrogel electrolyte.

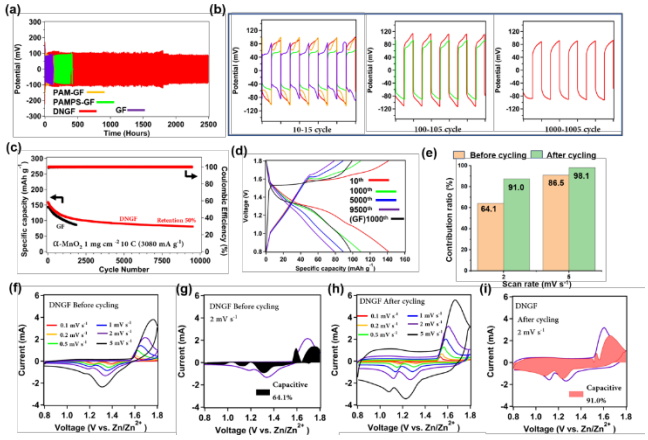

Figure. 5 (a) Cyclic stability of symmetric cells with different separators. (b) Details of voltage profiles corresponding to symmetric cell tests. (c) Zn || MnO_2 battery performance under low areal capacity. (d) Zn || MnO_2 battery voltage profiles at the 10th (red), 1000th (green), 5000th (blue), and 9500th (purple) cycle using DNGF as a separator. The black line is the voltage profile of the Zn-MnO_2 battery at the 1000th cycle in a Zn || MnO_2 battery using glass fiber as the separator. (e) Normalized capacitive contribution ratio of the DNGF separated Zn || MnO_2 battery at different scan rates. (f) CV curves of the DNGF separated Zn || MnO_2 battery before cycling. (g) Capacitive contribution of the DNGF separated Zn || MnO_2 battery to the total charge storage at 2 mV s^{-1} before cycling. (h) CV curves of the DNGF separated Zn || MnO_2 battery after cycling. (i) Capacitive contribution of the DNGF separated Zn || MnO_2 battery to the total charge storage at 2 mV s^{-1} after cycling.

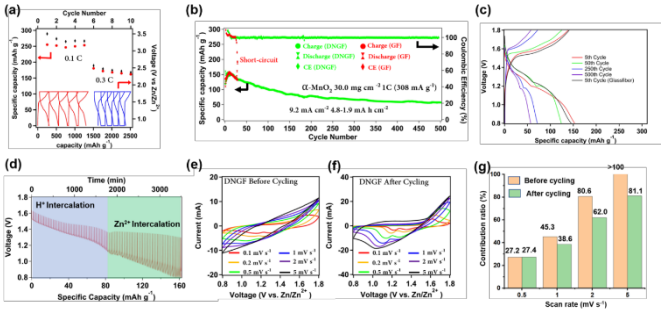

Figure. 6 Performance of Zn || MnO_2 batteries with high-capacity MnO_2 cathodes. (a) Low-rate performance of DNGF separated Zn || MnO_2 batteries, and the voltage profiles are inset within the figure. (b) Cyclic stability of high-mass loaded Zn || MnO_2 batteries at charge/discharge rate of 1 C. (c) Voltage profiles of the Zn || MnO_2 battery at the 5th (red), 50th (green), 250th (blue), and 500th (purple) cycle using DNGF as a separator. The black line is the voltage profile of the Zn || MnO_2 battery at the 5th cycle in a cell using glass fiber as a separator. (d) GITT measurement of the DNGF separated Zn || MnO_2 battery. CV curves of the DNGF separated Zn || MnO_2 battery (e) before and (f) after cycling. (g) Normalized capacitive contribution ratio of the DNGF separated Zn || MnO_2 batteries at different scan rates.

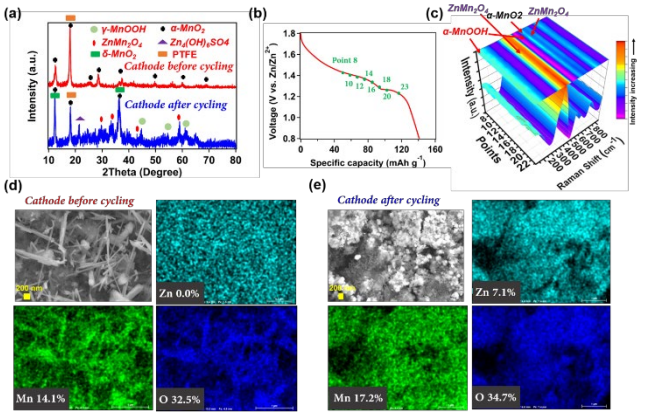

Figure. 7 Characterization of the MnO_2 cathode. (a) XRD patterns of the HCM cathode before and after cycling, corresponding to Figure 6. (b) Voltage profile of an independent galvanostatic discharge test for the HCM cathode after cycling. The inset points correspond to (c) in-situ Raman spectroscopy measurement during the discharge test. SEM and EDS images of HCM cathode (d) before and (e) after cycling.